Time-resolved imaging of bound and dissociating nuclear wave packets in strong-field ionized iodomethane

Journal:	*Physical Chemistry Chemical Physics*
Manuscript ID	CP-ART-11-2018-007032.R1
Article Type:	Paper
Date Submitted by the Author:	05-Jan-2019
Complete List of Authors:	Malakar, Yubaraj; Kansas State University, Physics Pearson, III, Wright; Kansas State University, Physics Zohrabi, Mohammed; Kansas State University, Physics Kaderiya, Balram; Kansas State University, Physics Pandiri, Kanaka; Kansas State University, Physics Ziaee, Farzaneh; Kansas State University, Physics Xue, Shan; Kansas State University, Physics Le, Anh-Thu; Kansas State University, Physics Ben-Itzhak, Itzik; Kansas State University, Physics Rolles, Daniel; Kansas State University, Physics Rudenko, Artem; Kansas State University, Physics

Time-resolved imaging of bound and dissociating nuclear wave packets in strong-field ionized iodomethane

Y. MALAKAR[1], W. L. PEARSON[1], M. ZOHRABI[1,2], B. KADERIYA[1], KANANKA RAJU P.[1], F. ZIAEE[1], S. XUE[1,3], A.T. LE[1,4], I. BEN ITZHAK[1], D. ROLLES[1], A. RUDENKO[1]

[1]J.R. Macdonald Laboratory, Department of Physics, Kansas State University, Manhattan, KS 66506, USA
[2]University of Colorado, Boulder, CO 80309, USA
[3]School of Nuclear Science and Technology, Lanzhou University, Lanzhou 730000, China
[4]Department of Physics, Missouri University of Science and Technology, Rolla, MO 65409, USA

Abstract: We report the results of a time-resolved coincident ion momentum imaging experiment probing nuclear wave packet dynamics in the strong-field ionization and dissociation of iodomethane (CH_3I), a prototypical polyatomic system for photochemistry and ultrafast laser science. By measuring yields, kinetic energies, and angular distributions of $CH_3^+ + I^+$ and $CH_3^+ + I^{++}$ ion pairs as a function of the delay between two 25-fs, 790-nm pump and probe pulses, we map both, bound and dissociating nuclear wave packets in intermediate cationic states, thereby tracking different ionization and dissociation pathways. In both channels, we find oscillatory features with a 130-fs periodicity resulting from vibrational motion (C-I symmetric stretch mode) in the first electronically excited state of CH_3I^+. This vibrational wave packet dephases within 1 ps, in good agreement with a simple wave packet propagation model. Our results indicate that the first excited cationic state plays a key role in the dissociative ionization of CH_3I and that it represents an important intermediate in the sequential double and multiple ionization at moderate intensities.

Keywords: strong-field ionization, ultrafast lasers, coincident ion momentum imaging, Coulomb explosion, molecular dissociation

1. Introduction

Advances in ultrafast laser technology and particle detection techniques have significantly deepened our understanding of light-matter interactions and the ensuing dynamics on a molecular level, facilitating insights into light-induced physical, chemical, and biological processes. Fueled by the pioneering work of Nobel Laureate Ahmed Zewail, pump-probe spectroscopy with ultrafast lasers has opened up the field of femtochemistry.[1] In such measurements, the pump pulse initiates a reaction of interest by launching a molecular wave packet on certain neutral or ionic states, which is then probed by a synchronized probe pulse arriving after a variable time delay. Each delay between the pump and probe pulses results in a snapshot of the time-evolving process(es) at that moment in time. This enables time-resolved studies of molecular processes driven by ultrafast laser fields, including electronic, vibrational and rotational excitations, ionization, dissociation, Coulomb explosion, and bond rearrangement.[2, 3] Depending on the specific molecular target, the

wavelength, and the intensity of the laser pulse, molecules can be ionized by strong laser fields through different competing mechanisms. In the near-infrared (NIR) region, the dominant mechanisms typically evolve, with increasing intensity, from multiphoton, tunneling, and over-the-barrier ionization, which leave the molecule in a variety of bound or repulsive singly-charged final states, to double and multiple ionization. The latter two processes often result in the molecule breaking into several charged fragments in a process termed "Coulomb explosion" (CE). If multiple ionization and the ensuing breakup occur faster than the characteristic time scale of the nuclear motion, the resulting fragment momenta carry information about the molecular geometry at the moment of ionization.[4-8] This experimental approach, known as Coulomb explosion imaging (CEI), was originally developed for collisions of fast molecular beams with thin foils,[9] and later proved to be an efficient probe scheme for time-resolved experiments with ultrafast lasers.[10-15]

In this work, we apply the CEI technique to study strong-field induced ionization and dissociation of iodomethane (CH_3I). Being a relatively simple and well-characterized polyatomic molecule, CH_3I has served as a prototype system for investigations of photoinduced molecular dynamics for more than three decades[14, 16-32] and at wavelengths ranging from the infrared [33-46] to the hard X-ray domain.[47, 48] For example, CH_3I was recently used to demonstrate novel schemes to control photodissociation reactions through light-induced conical intersections,[37, 40] to address multi-electron effects via two-electron angular streaking,[46] and to study charge transfer processes following X-ray absorption in laser-dissociated molecules.[32, 49-51] These and other applications require a detailed quantitative understanding of the single and multiple ionization and dissociation of CH_3I in strong laser fields. While the ultraviolet dissociation of neutral CH_3I has been extensively studied in various pump-probe experiments,[14, 19, 21-23, 25, 26, 29-32, 52-54] its ionization and dissociation dynamics at near-infrared (NIR) wavelengths has been mainly characterized in single-pulse measurements.[33-36,38,41,46] These studies are complemented by recent pump-probe experiments, which utilized extreme-ultraviolet transient absorption to map vibrational motion[42] and dissociative ionization[43] of CH_3I triggered by intense ultrashort NIR fields. In addition, measurements aimed at characterizing the alignment- and orientation-dependence of the ionization and fragmentation process by employing impulsive alignment[44,45] and phase-controlled two-color laser fields[39] have been performed. However, despite these efforts, the current understanding of fundamental issues such as the role of different molecular orbitals, branching ratios of different fragmentation channels, the dependence of ionization and dissociation probability on molecular orientation, and ionization enhancement at certain internuclear separations is far from being complete.

In this work, a combination of a NIR pump-probe arrangement (employing two 25-fs, linearly polarized, 790-nm pulses) and Cold Target Recoil Ion Momentum Spectroscopy (COLTRIMS)[55-57] is used to map the spatio-temporal evolution of bound and dissociating nuclear wave packets created by strong-field ionization of CH_3I. This is realized by measuring the yields, kinetic energies, and angular distributions of ion pairs resulting from the $CH_3^+ + I^+$ and $CH_3^+ + I^{++}$ two-body breakup channels, as a function of pump-probe delay. Coincident detection of both ionic fragments allows for unambiguous identification of the reaction final charge state after the probe

pulse and, thus, considerably simplifies disentangling different ionization and fragmentation pathways. While for delay-independent channels, our results closely resemble the kinetic energy release (KER) distributions obtained in earlier single-pulse measurements,[36,38,41] we observe a pronounced oscillatory structure at lower KER values in both channels, which, to the best of our knowledge, was not previously discussed in the literature. Based on the oscillation frequency, we interpret this feature as a signature of coherent vibrational motion in the excited $\tilde{A}^2A_1$ state of CH_3I^+. Within 1 ps, we observe a dephasing of this vibrational wave packet, in good agreement with the results of a simple wave packet propagation simulation. Furthermore, we visualize the dominant dissociative ionization pathways for fragments emitted parallel and perpendicular to the laser polarization direction, show that they have distinctly different asymptotic dissociation energies, and discuss the relation between these findings and the results of earlier single-pulse measurements on aligned and randomly oriented molecules.

2. Experimental Methodology

The concept of the present experiment is illustrated in Fig. 1. The pump pulse ionizes a neutral CH_3I molecule, predominantly populating either bound or repulsive cationic and dicationic states. The probe pulse further ionizes the system, which fragments along one of the higher-lying repulsive potential energy curves (PEC). Since more than one final-state PEC can yield a particular charge state pair, precise reconstruction of the nuclear wave packet in the intermediate state would require detailed modeling of the ionization by the probe pulse and the corresponding deconvolution of the experimental data. Nevertheless, even though both dicationic and tricationic potential curves were shown to deviate from purely Coulombic ones,[36] the KER for these final states measured as function of pump-probe delay still carries information about the C-I separation ($R_{C\text{-}I}$), in particular, at large $R_{C\text{-}I}$. In this work, we focus on the qualitative analysis of the doubly and triply charged final states resulting in a two-body break-up. Those

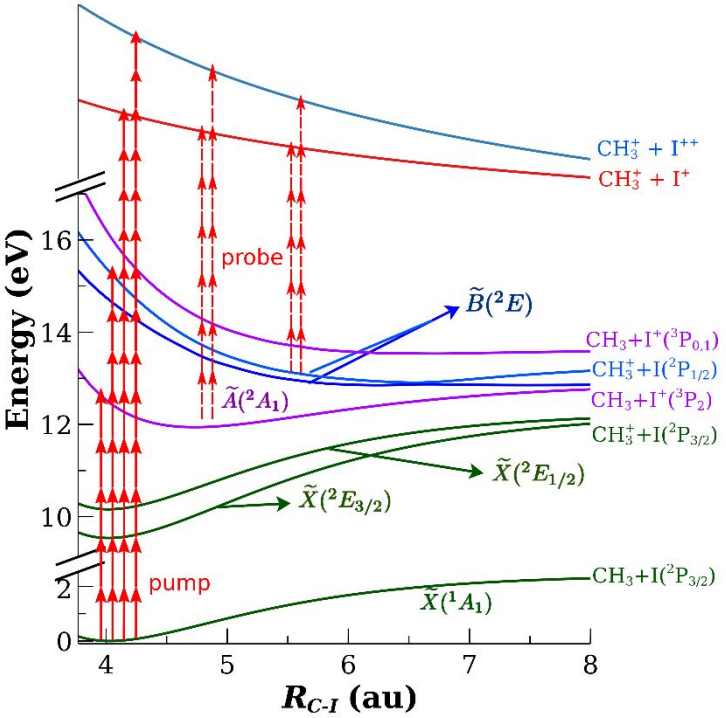

Fig. 1: Schematics of the pump-probe experiment and relevant potential energy curves (PEC) of CH_3I along the C-I bond. The bound states (the neutral ground state, the cationic ground state, and first excited states) are simulated by using a Morse potential with parameters based on spectroscopic data.[42,58-60] The repulsive cationic PECs are calculated using the MOLCAS quantum chemistry package,[61] while the dicationic and tricationic PEC are sketches shown to illustrate the probe step.

events that, after the probe pulse, result in a bound dication or that end up in bound or dissociating singly-charged states will be subject of a separate publication.[62]

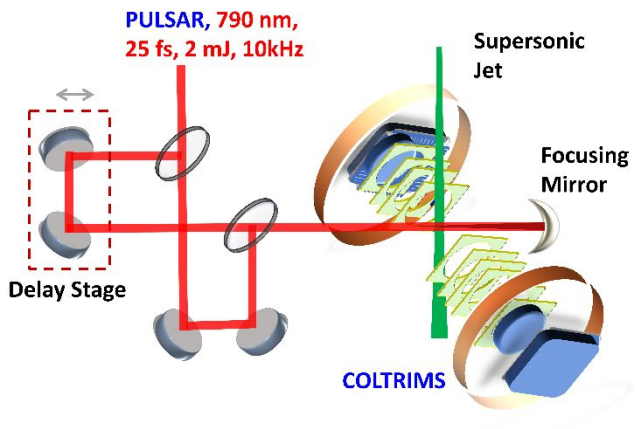

Fig. 2: Sketch of the setup of the time-resolved coincident momentum imaging experiment.

The experimental setup for NIR pump-probe experiments using coincident ion momentum imaging is sketched in Fig. 2. The linearly polarized output of a Ti:Sapphire chirped-pulse amplification laser system known as PULSAR[63] (repetition rate 10 kHz, central wavelength 790 nm, pulse duration 25 fs (full width at half maximum in intensity), maximum pulse energy 2 mJ) is fed into a Mach-Zehnder type interferometer with one arm variable in length, providing two identical NIR pulses separated by an adjustable time delay. For the measurements reported here, the delay was varied between -0.5 and 9.5 ps. After recombining, both pulses are focused by an on-axis spherical concave mirror with 7.5 cm focal length onto a supersonic molecular beam in the center of a Cold Target Recoil Ion Momentum Spectrometer (COLTRIMS).[64]

To minimize clustering during the beam expansion, we used a pure iodomethane sample without a carrier gas. The temperature of the molecular beam is estimated to be 30 K by fitting the velocity distribution of CH_3I^+ parent ion with a Maxwell probability distribution. All the results presented here are obtained with the polarization of both laser pulses parallel to the spectrometer axis and perpendicular to the molecular beam. The peak laser intensity is determined from a calibration measurement of the Ne^+ ion momentum distribution, which displays a characteristic kink at the recoil momentum value corresponding to emission of photoelectrons with $2U_p$ kinetic energy (where the ponderomotive energy U_p is the average quiver energy of the free electron in the laser field), which represents the transition from direct to rescattered electrons, as detailed in[65].

The COLTRIMS spectrometer has been described in more detail elsewhere.[64] Briefly, the molecular ions and ionic fragments produced by the interaction of the intense NIR pulses with the molecules in the gas target are accelerated towards a microchannel plate (MCP) detector equipped with a time and position resolving delay-line anode by applying a uniform extraction field of 48.5 V/cm. The analog MCP and delay line signals containing the time-of-flight and position information of the detected ions are amplified, processed by constant fraction discriminators (CFD), and recorded by a multi-hit time-to-digital converter (TDC) on an event-by-event basis for further offline analysis. From this recorded information, the full three-dimensional momentum of each detected ion is calculated (see[56, 57] for details).

3. Results and Discussion

3.1. Identification of CH_3I fragmentation channels

At the peak intensities used in this study (1.5×10^{14} – 4×10^{14} W/cm^2), CH_3I is singly or multiply ionized and can break into several neutral and ionic fragments. Only the ionic products are recorded in our experiment. Fig. 3 displays the ion time-of-flight (TOF) spectrum (a) and the photoion-photoion coincidence (PIPICO) spectrum (b) obtained from the NIR strong-field ionization of CH_3I by a pair of 4×10^{14} W/cm^2 pulses in a pump-probe measurement (integrated over all delays ranging from -0.5 to 9.5 ps). Since the sum momentum of the absorbed photons and emitted electron is much smaller than the momenta of the nuclei, sharp lines in the PIPICO spectrum represent coincident ion pairs that satisfy momentum conservation and, thus, originate from laser-induced two-body breakup of the parent molecule. Two of such two-body channels, $CH_3^+ + I^+$ and $CH_3^+ + I^{++}$, can be clearly identified, as shown in the inset of Fig. 3. The long "tail" that extends from the former channel [marked "1" in Fig. 3(b)] all the way to the main

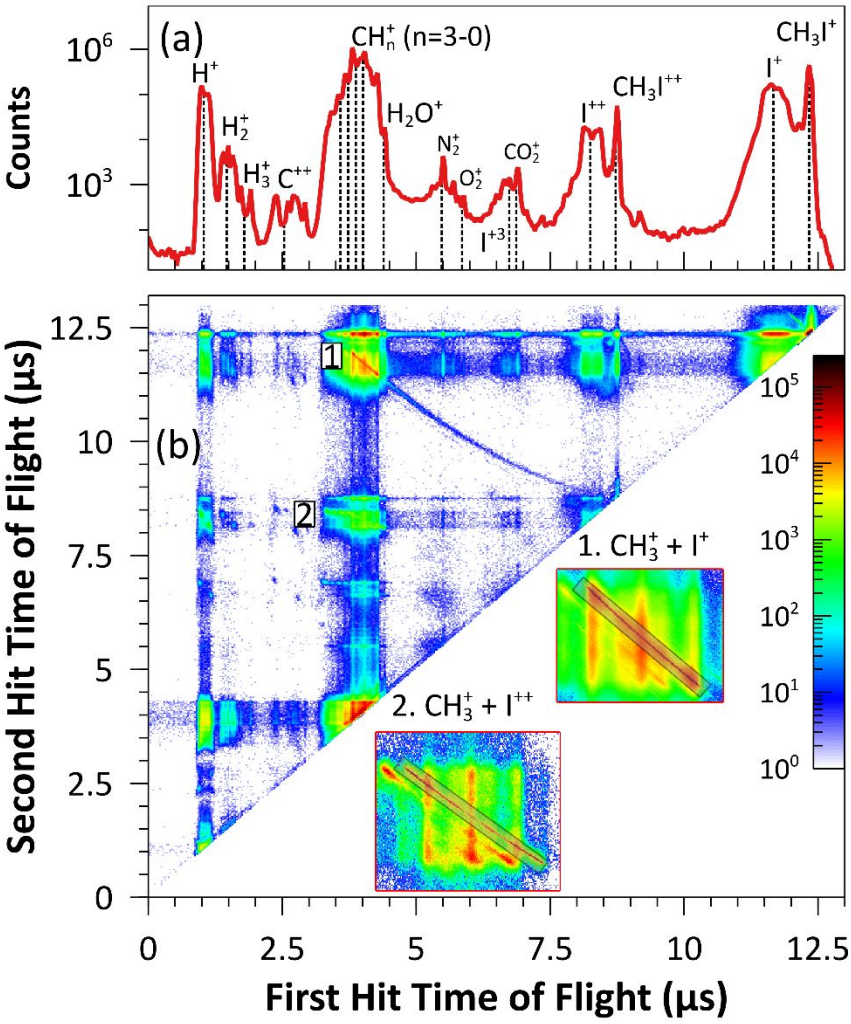

Fig. 3: (a) Ion time-of-flight (TOF) spectrum and (b) photoion-photoion coincidence (PIPICO) plot for strong-field ionization and fragmentation of CH_3I by a pair of identical 4×10^{14} W/cm^2 NIR pulses. The data are integrated over a delay range from -0.5 to 9.5 ps. Dashed vertical lines in (a) show the TOF values for the corresponding ionic species with zero momentum along the spectrometer axis. The labels 1 and 2 indicate the two main channels of interest, $CH_3^+ + I^+$ (1,1) and $CH_3^+ + I^{++}$ (1,2). The insets show the zoomed-in regions around these channels. The weaker PIPICO features that are parallel to these lines correspond to the breakup channels where the methyl group has lost one or several protons or hydrogen atoms. Broad vertical structures result from "false" coincidences, i.e., ion pairs originating from two different target molecules.

diagonal originates from the dissociation in flight of a metastable CH_3I^{++} dication (see Ref.[66]). Note that no sharp lines in the PIPICO spectrum are observed in the region containing H^+, H_2^+, and H_3^+ ions. This indicates that, under our experimental conditions, deprotonation or H_2^+ / H_3^+ elimination reactions following double or multiple ionization of CH_3I predominantly result in molecular breakup into three or more fragments.

When discussing the outcome of the pump-probe experiment in the following, we will mainly focus on the two-body breakup channels highlighted in Fig. 3(b). Following the convention used in[34, 36, 41], we will sometimes refer to $CH_3^+ + I^+$ and $CH_3^+ + I^{++}$ channels as (1,1) and (1,2), respectively. In order to investigate the pathways leading to these final states and to elucidate the underlying nuclear wave packet dynamics, we analyze the delay dependence of the corresponding ion kinetic energies and angular distributions. For this analysis, we consider only those ion pairs, which fulfil the momentum conservation condition for all three momentum components.

3.2. Pump-probe delay dependence of the $CH_3^+ + I^+$ channel

Fig. 4(a) shows the dependence of the KER distribution for the $CH_3^+ + I^+$ channel on the time delay between two 1.5×10^{14} W/cm^2 NIR pump and probe pulses. Three characteristic features can be distinguished in the spectrum. First, there are two strong, delay-independent bands between 4 and 6 eV. Second, a delay-dependent structure, marked by the superimposed dashed lines in Fig. 4(a), is discernible, which evolves towards lower KER with increasing pump-probe delay. Third, an oscillatory structure in the KER range between 3-4 eV is visible. In the following, we will discuss the dominant pathways resulting in these three contributions.

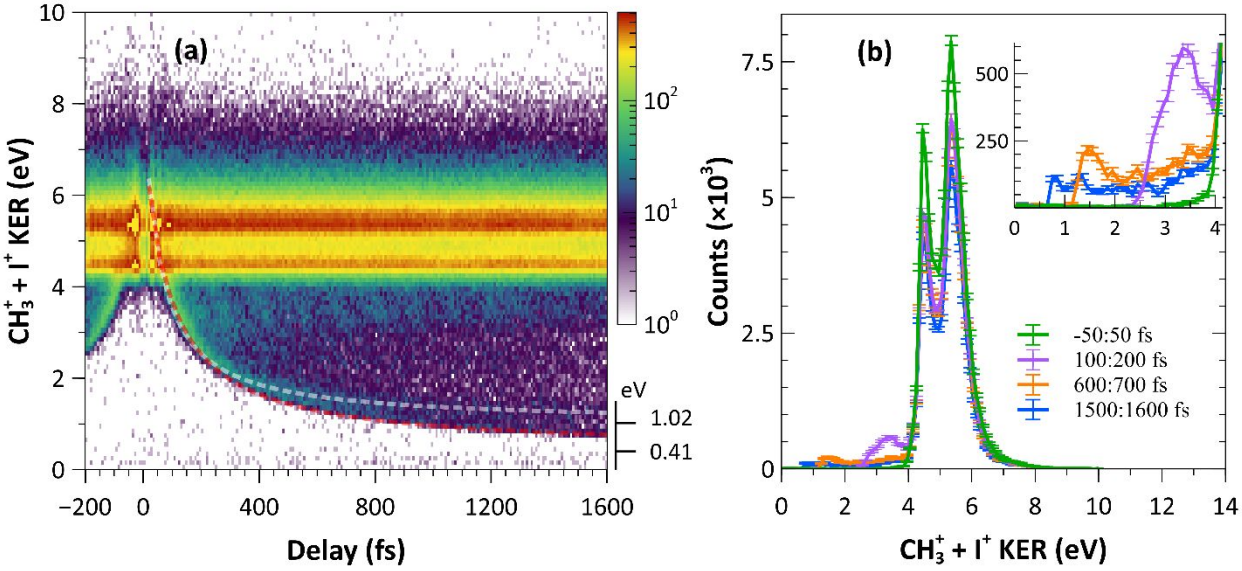

Fig. 4: (a) Delay-dependent KER distribution of the $CH_3^+ + I^+$ breakup channel measured at a peak intensity of pump and probe pulses of 1.5×10^{14} W/cm^2. The red and white dashed lines are the results of classical Coulomb explosion simulations, with the numbers in the lower right corner indicating the asymptotic KER values used for these simulations (see text). **(b)** KER distribution of the $CH_3^+ + I^+$ channel for four different delay intervals. The inset shows an enlarged view of the low-KER region.

3.2.1. Delay-independent KER bands

The two delay-independent bands, peaked at a KER of 4.5 and 5.4 eV, represent the dominant contribution to the spectrum, as can be seen in Fig. 4(b), where the KER distributions for four narrow pump-probe delay intervals are shown. They mainly originate from a Coulomb explosion that occurs within either the pump or the probe pulse alone. Therefore, these features do not show any dependence on the delay between the two pulses, apart from the region close to zero delay, where the ionization rate is strongly structured due to constructive or destructive interference between pump and probe pulses when they overlap in time. The apparent minimum right around zero delay is due to a sudden, large increase in the dead time of the data acquisition system when the count rate surpasses a critical value due to the strong ionization at the maximum of the constructive interference between pump and probe pulses. The KER distribution for this overlap region [green curve in Fig. 4(b)] is nearly identical to the corresponding spectrum obtained with either the pump or the probe pulse alone.

The observed KER distribution for these two bands is in good agreement with previously reported results for strong-field induced Coulomb explosion of CH_3I with 50 fs, 800-nm laser pulses at 10^{13} to 10^{14} W/cm^2.[36, 38] According to calculations presented by Corrales *et al*. [36], the peak at 4.4-4.5 eV for the (1,1) channel corresponds to a fragmentation via the dicationic electronic ground state, asymptotically converging to the CH_3^+ and $I^+(^1D_2)$ limit, while the peak at 5.2-5.4 eV includes contributions from several higher-lying electronic states corresponding to the excited states ($^1S_0$, $^1D_2$, $^3P_0$, $^3P_1$) of the I^+ ion after the fragmentation. In particular, it was noted that these KER values are lower than the value of 6.73 eV, which is expected when considering a purely Coulombic repulsion corresponding to the equilibrium distance of the neutral CH_3I. Corrales *et al.* attributed this deviation to the non-Coulombic character of the potential energy curves for the CH_3I^{2+} species at small C-I distances, which leads to a weakly bound minimum and, thus, a smaller KER. This picture is consistent with the detection of a significant amount of bound CH_3I^{2+} [see Fig. 3(a)], with some of the metastable dications dissociating in flight, as reflected by the long tail of the main coincidence line in Fig. 3(b). An earlier study by Liu *et al.*[34] provided an alternative explanation for the lower KER values based on the concept of enhanced ionization occurring at an increased C-I distance in the molecular cation. However, it is noteworthy that Liu *et al.*[34] as well as a later study of Zhang *et al.*[41] reported central KER values of about 3.7 – 4 eV for the $CH_3^+ + I^+$ fragmentation channel, which is significantly lower than the KER values reported in the more recent studies[36, 38] and those obtained for the delay-independent CE bands in the present work. The key difference between these two groups of measurements is likely the longer pulse duration used in the former two measurements (180 fs[34] and 100 fs [41] versus 50 fs[36, 38] and 25 fs pulses used in this work). The longer pulse duration leaves more time for nuclear wave packets in intermediate states to propagate to larger internuclear separations before the second ionization occurs, resulting in lower KER. As we show in the following, our pump-probe experiment reveals a delay-dependent structure, which appears exactly in the KER region of 3 – 4 eV, suggesting that the two explanations for the observed KER values by Liu *et al.* and Corrales *et al*. are complimentary rather than contradictory. A signature of this effect can be clearly seen in the KER distribution for

100-200 fs delay window [purple curve in Fig. 4(b)], where a pronounced shoulder centered at ~3.5 eV appears. As will be detailed in the following two sections, part of the nuclear wave packet at larger delays remains bound in the electronically excited cationic state, whereas another part dissociates, resulting in the low-KER portion of the spectrum shown in Fig. 4.

3.2.2. Dissociative wave packets

In addition to the delay-independent bands, a delay-dependent structure marked by the dashed lines in Fig. 4(a) is clearly visible, which evolves towards lower KER with increasing pump-probe delay. The time-evolution of this feature is reflected in the appearance of low-KER peaks in the KER distributions at different delays shown in Fig. 4(b). It is completely absent in the overlap region [green curve in Fig. 4(b)], appears as a pronounced broad peak at 1.5 eV in the intermediate delays range (orange curve), and splits into two low-energy peaks at largest delays (blue curve). We attribute this structure to pump-probe events where the pump pulse dissociatively ionizes the neutral molecule into a CH_3^+ and I or a CH_3 and I^+ pair (which is often denoted as (1,0) and (0,1) dissociation, respectively), and the probe pulse further ionizes the system such that the dissociating wave packet is projected on a strongly repulsive, dicationic potential energy curve. The longer the delay between the pump and the probe pulses, the larger the separation between dissociating fragments created by the pump pulse, and, thus, the smaller the additional kinetic energy gained when the wave packet is projected onto the dicationic potential energy curve. For a purely Coulombic potential, this additional kinetic energy scales with $1/R$, where R is the separation between the two charges at the time of the second ionization. This relatively simple picture, which results in characteristic descending lines observed in numerous pump-probe experiments (see e.g.[14, 67-69]), is corroborated by classical Coulomb-explosion simulations [dashed lines in Fig. 4(a)] assuming point-like charges located at the position of the iodine and carbon atoms. The dissociating fragments produced by the pump pulse are assumed to travel with constant kinetic energies during the time between the pump and the probe. These energies (and, subsequently, the velocities of the fragments) are calculated via momentum conservation from the experimentally observed asymptotic KER values at long pump-probe delays (~10 ps), where the contribution of Coulomb repulsion becomes negligible. We used the KER values of 0.41 and 1.02 eV (indicated by tick marks) for the red and white curves, respectively. The asymptotic KER values obtained in our pump-probe experiment are consistent with the kinetic energies of the low-energy CH_3^+ and I^+ ions in our single pulse measurements and also with the kinetic energy values of 0.37 and 0.91 eV for CH_3^+ in the (1,0) channel, and 0.07 eV for I^+ in the (0,1) channel reported by Liu *et al.*[34] The additional energy gained after the ionization by the probe pulses is assumed to be given by the Coulomb repulsion at a given $R_{C\text{-}I}$ (i.e., proportional to $1/R_{C\text{-}I}$) and is added to the KER of the initial dissociation. It should be noted that the kinetic energy distributions for these dissociative ionization channels are rather broad, such that the simulated lines corresponding to the peak values should be considered only as an indication of the dominant trends.

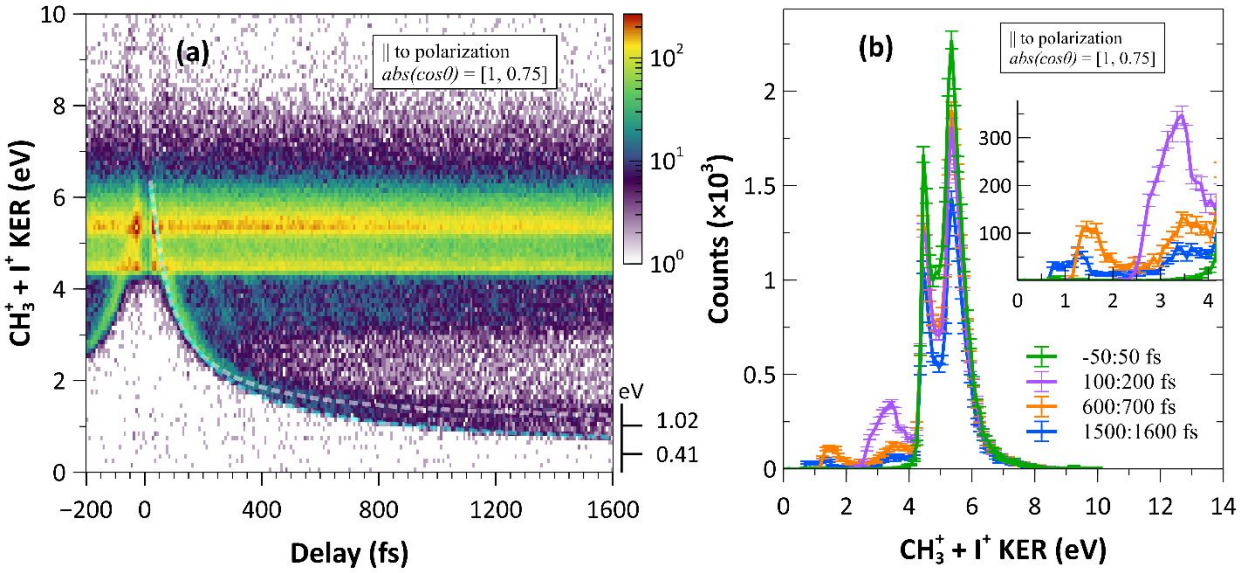

Fig. 5: Same as Fig. 4 but selecting only those events where the ion pairs are emitted parallel to laser polarization, i.e., in a cone with an opening angle θ with $|cos\theta| > 0.75$.

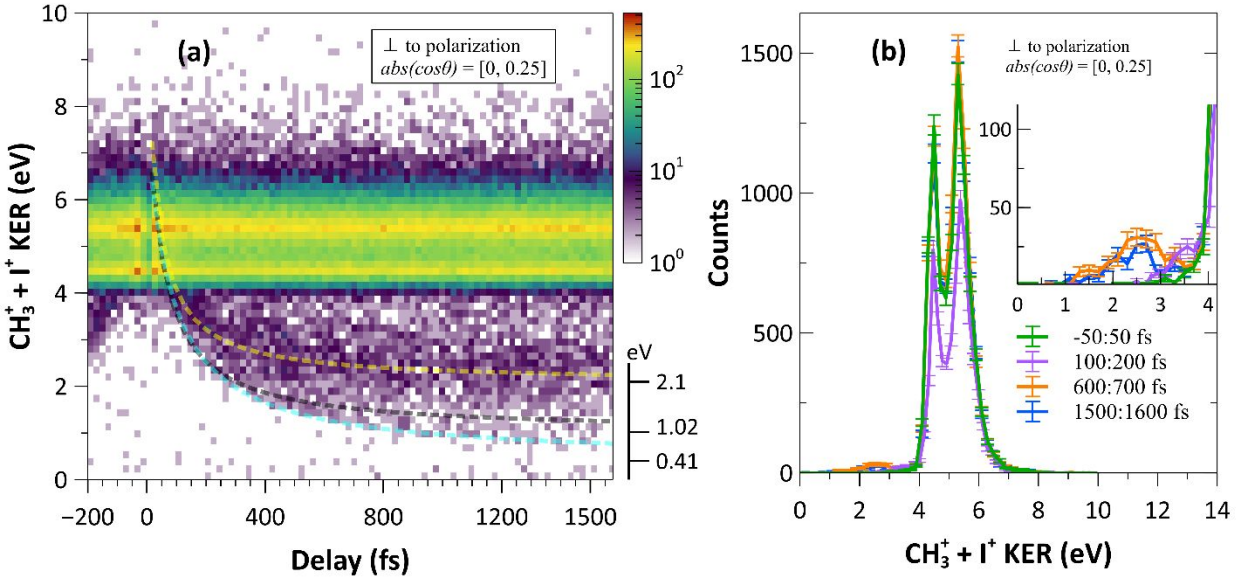

Fig. 6: Same as Fig. 4 but for ion pairs emitted perpendicular to the laser polarization *(*$|cos\theta| < 0.25$).

Additional insight can be gained when considering the angular distributions of the ionic fragments

with respect to the polarization direction of the laser pulses, e.g., by plotting the delay-dependent KER distribution in Fig. 4 only for those fragments emitted parallel or perpendicular to the polarization direction, as shown in Fig. 5 and 6, respectively. Here, it becomes apparent that the dominant dissociation channels with lowest asymptotic KER are strongly anisotropic with a maximum along the polarization direction, while a weaker band with higher KER (~2 – 2.5 eV) is only visible when selecting ions emitted perpendicular to the polarization direction. A more explicit picture of angular distributions of different pathways is shown in Fig. 7, where the yield of the $CH_3^+ + I^+$ channel in the 1.3 – 1.6 ps delay interval is shown as a function of the cosine of the fragment emission angle θ with respect to the laser polarization and the KER. From this graph, it can be clearly seen that while most of the fragmentation channels peak at $cos\theta = \pm 1$ (i.e., parallel to the laser polarization), the KER region between 2 and 3 eV manifests a more isotropic angular distribution, with a significant contribution at $cos\theta$ values close to zero (perpendicular to the polarization direction).

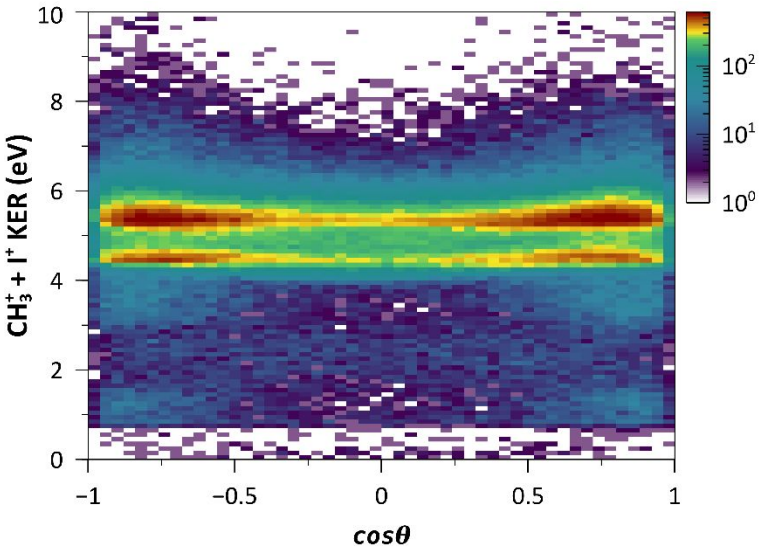

Fig. 7: Measured yield of the $CH_3^+ + I^+$ channel, integrated over a delay window of 1.3 to 1.6 ps, as a function of the KER and the emission angle θ with respect to the laser polarization.

While a more detailed experimental and theoretical analysis of dissociative ionization pathways observed in the present experiment will be presented elsewhere,[62] a brief overview of the major channels contributing to the low-energy (KER < 3 eV) part of the spectra shown in Figs. 4 – 6 is provided in the following. The non-coincident low-energy I^+ fragments resulting from the (0,1) channel in our single-pulse measurements exhibit a pronounced peak centered at 0.11 eV, a smaller peak at 0.02 – 0.04 eV, and a weaker broad shoulder centered at 0.22 eV. This structure of the spectrum remains nearly unchanged for all intensities studied ($1.5 \times 10^{14} – 4 \times 10^{14}$ W/cm^2). In our pump-probe measurements, the probe-pulse ionization of the molecule dissociating via the two lower-energy channels results in the descending bands with an asymptotic KER of ~1 eV and 0.4 eV, respectively (shown as dashed lines in Figs. 4 – 6), whereas the pathway originating from the 0.22 eV I^+ energy yields an asymptotic KER of 2.1 eV, which is clearly visible only for the fragments emitted perpendicular to the laser polarization in Fig. 6(a). The CE simulation assuming a KER value of 2.1 eV [shown as a yellow dashed line in Fig. 6(a)] matches well the delay-dependent KER of this feature.

For a particular dissociative ionization channel, the angular distribution of the resulting fragments is mainly determined by two factors. The first one is the dependence of the ionization probability on the initial orientation of the molecule.[44,45,70] The second is the angular dependence of the dissociating transition in the cation, if the ionization itself does not directly populate the dissociative state.[44, 45] Furthermore, a direct link between the fragment angular distributions and the orientation of the molecular axis relies on the validity of the axial recoil approximation.[71] For strong-field ionization of CH_3I at NIR wavelengths, it was recently shown, both experimentally and theoretically, that the non-dissociative ionization yield, which is dominated by electron removal from the (degenerate) π-type highest occupied molecular orbital (HOMO) (which corresponds to the population of the spin-orbit split ionic ground state, see Fig. 1), reaches its maximum when the laser polarization is perpendicular to the molecular axis.[44, 45, 70] The same studies conclude that for molecules aligned parallel to the laser polarization, the ionization of the σ-type HOMO-1 orbital (leaving the ion in the excited $\tilde{A}^2A_1$ state) provides the dominant contribution. Since the production of singly-charged CH_3^+ and I^+ fragments observed in[44, 45] peaked when the molecules were aligned parallel to the laser polarization, it was suggested that the dissociative ionization of CH_3I mainly proceeds via the excited $\tilde{A}^2A_1$ cationic state (denoted as "$\tilde{A}$ state" in Fig.1). Our results for the dominant low-energy dissociation channels (KER < 2 eV) support this interpretation, which is at odds with the channel assignments made in[34, 35, 41], where the observed dissociative ionization energies are explained in terms of various multiphoton transitions from the spin-orbit split ionic ground state. The dominance of the $\tilde{A}$-state contribution to the dissociative ionization of CH_3I is also predicted by our calculation employing a combination of molecular ADK theory with the numerical solution of the TDSE for the nuclear wave packet propagation in the cationic potential curves.[62] Specifically, we assign the (0,1) channels producing I^+ ions with ~0.11 eV and ~0.03 eV energies to single-photon transitions from the $\tilde{A}$ state to the $\tilde{B}$ (^2E) $(CH_3 + I^+(^3P_2)$ and to higher-lying $CH_3 + I^+(^3P_{0,1})$ repulsive states, respectively. All of these transitions occur at C-I distances beyond the Franck-Condon region while the nuclear wave packet is propagating outwards on the $\tilde{A}$-state potential, which results in rather low kinetic energies of the corresponding fragment ions.[62] They are preferentially emitted along the polarization direction since, according to our simulation,[62] the dominant contribution to these channels comes from parallel transitions.

The dissociative ionization pathway(s) resulting in the appearance of a pronounced dissociating band centered at a KER value of ~ 2.5 eV for the fragments emitted perpendicular to the laser polarization in Fig. 6 require further investigation. Possible scenarios for this channel include an initial ionization to the ionic ground state, or a perpendicular dissociating transition upon the population of the $\tilde{A}^2A_1$ state. The appearance of such contribution can, in fact, also be observed in Fig. 2 of Ref.[36], even though (0,1) and (1,0) channels are not discussed in that work.

Besides the (0,1) channel producing I^+ ions with a neutral CH_3 partner, the (1,0) transitions resulting in the creation of CH_3^+ fragments also contribute to the low-energy part of the spectrum. The kinetic energy distribution of the non-coincident CH_3^+ ions detected in our single-pulse

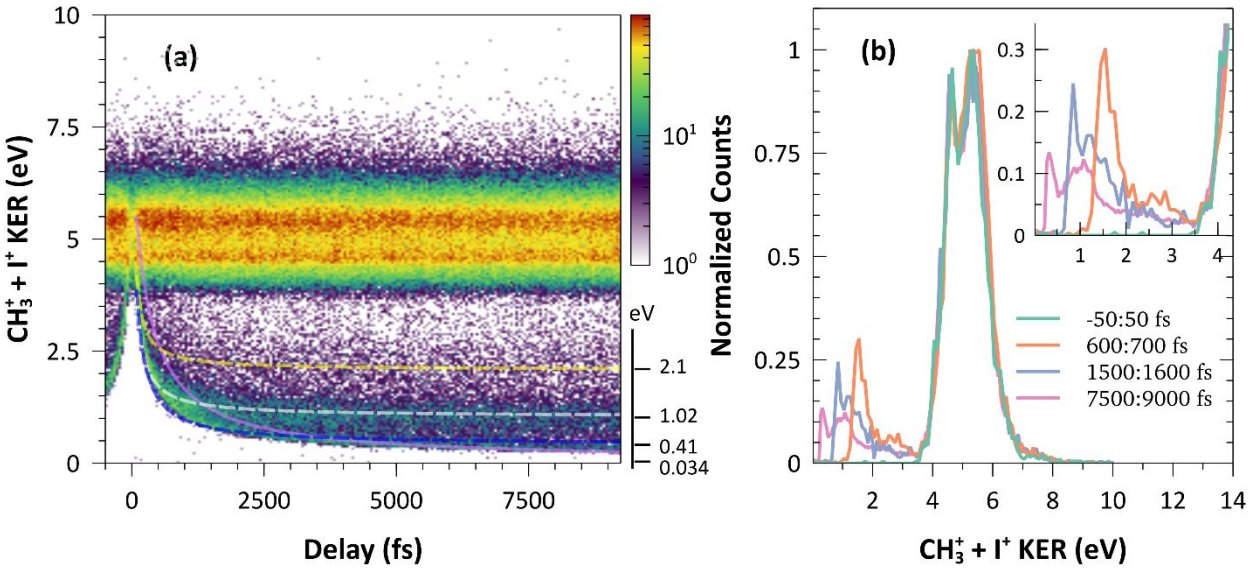

Fig. 8: Same as Fig. 4 but for higher peak intensity (4×10^{14} W/cm^2) of both pump and probe pulses and for a longer delay range.

measurements is dominated by low-energy fragments (CH_3^+ energies below 0.05 eV). It also manifests a broad shoulder at ~0.35 – 1 eV kinetic energies, which rapidly decreases towards higher energies. The (1,0) dissociative ionization events from the latter region (corresponding to the asymptotic KER of 0.39 – 1.1 eV) contribute to the descending band between the two dashed lines in Figs. 4 and 5. According to our analysis detailed in[62], they originate from single-photon coupling between the $\tilde{A}$ and the $\tilde{B}(^2E)$ $(CH_3{}^+ + I(^2P_{1/2})$ states, which is consistent with fact that the angular distribution of the corresponding band peaks along the laser polarization direction. As for the dominant low-energy peak in the (1,0) channel, it can be produced by internal conversion between the $\tilde{A}$ and $\tilde{X}^2E_{1/2}$ states.[58, 72] Since this process occurs on a nanosecond time scale, it does not contribute to our pump-probe data. Several net zero-photon processes involving downward transitions to the $\tilde{X}^2E_{1/2}$ state can also contribute to this structure.[62] The contribution from this nearly zero-KER pathway can be better visualized using the data from a longer delay scan, which are presented in Fig. 8.

Fig. 8(a) displays the delay-dependent KER distribution of the $CH_3^+ + I^+$ channel measured in a -0.5 – 9.5 ps delay window using more intense, 4×10^{14} W/cm^2 NIR pump and probe pulses, while Fig. 8(b) displays the KER distributions for four different, narrow delay intervals within this range. As can be seen from the KER distribution at large delays [magenta curve in Fig. 8(b)], the part of the dissociating wave packet around 1 eV KER significantly broadens, reflecting the overlapping contributions from (0,1) and (1,0) channels discussed above. The lower KER feature at this large delay is centered close to the asymptotic value of 0.4 eV, also in good accord with the assignments made above. However, from the delay-dependent plot in Fig. 8(a), it is clear that the lowest-energy component of the dissociating wave packet did not yet reach its asymptotic KER values even at 10

ps delay, suggesting a contribution from a very low-energy dissociation via the (1,0) channel. This is highlighted by the classical CE simulation assuming a CH_3^+ energy of 0.03 eV (asymptotic KER 0.034 eV) shown as a magenta line in Fig. 8(a).

3.2.3. Vibrational wave packet in the cationic $\tilde{A}$ state

In addition to the features with strongly delay-dependent KER discussed above, an oscillatory structure in the KER range between 3 and 4 eV is clearly visible in Figs. 4(a) and 5(a). This structure only appears in the direction parallel to the laser polarization [Fig. 5(a)], and the periodic oscillations are clearly fading out over the displayed delay range.

A projection of the coincident $CH_3^+ + I^+$ ion yield in the KER region of 3 – 3.8 eV onto the delay axis is shown in Fig. 9(a) and displays a pronounced oscillation with ~130-fs period. The power

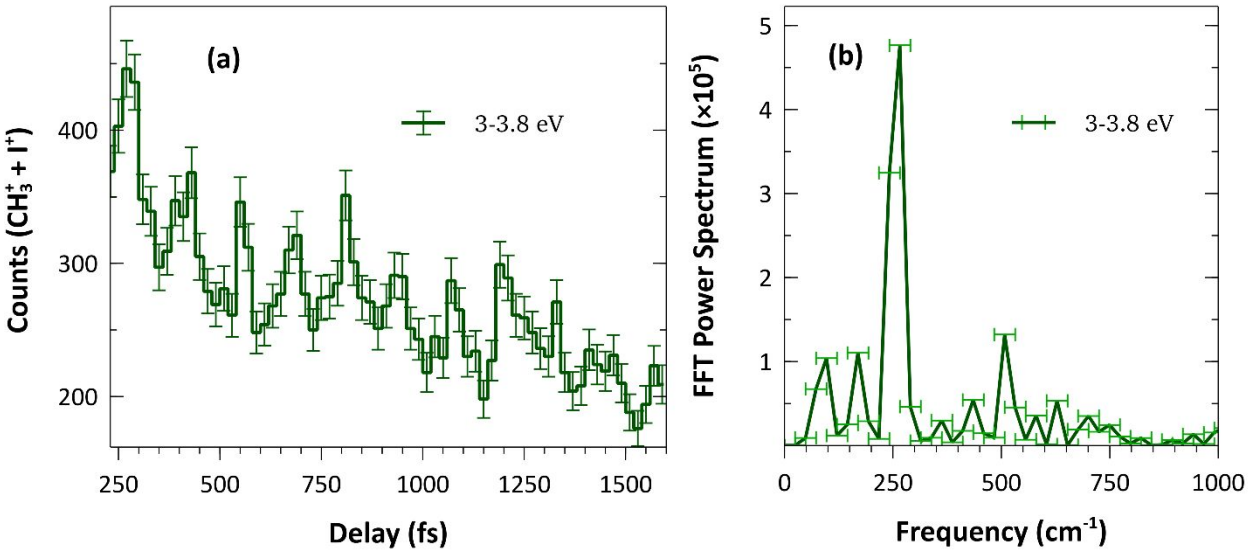

Fig. 9: (a) Delay dependence of the coincident $CH_3^+ + I^+$ ion yield in the 3 – 3.8 eV KER range. **(b)** Power spectrum obtained by a FFT of the data in panel (a).

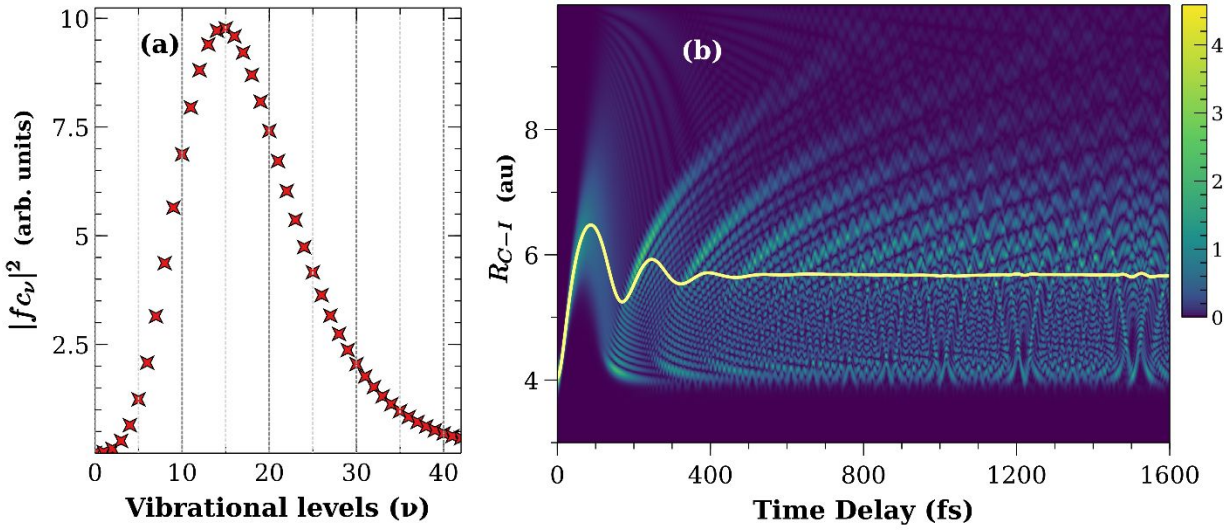

Fig. 10: (a) Calculated Franck-Condon vibrational state distribution. (b) Simulated probability density of the vibrational wave packet propagating on the $\tilde{A}$ state. The yellow line shows the corresponding time-dependent expectation value of the C-I internuclear separation.

spectrum resulting from a fast Fourier transformation (FFT) analysis of these data is presented in Fig. 9(b). It has a prominent peak centered at ~265cm^{-1} (within the ±45 cm^{-1} experimental uncertainty), slightly below the vibrational frequency of the C-I stretching mode ($v3$) in the excited $\tilde{A}$ state of CH_3I^+ (294 cm^{-1}). [59] This suggests that the pump pulse creates a coherent superposition of vibrationally excited states in the cationic $\tilde{A}$ state, which is then probed by CEI. The pronounced angular anisotropy of this channel, which can be observed in Figs. 5 and 6, supports this interpretation. Since the potential minimum of the $\tilde{A}$ state is shifted with respect to the neutral ground state (see Fig. 1), the created vibrational wave packet propagates towards larger C-I separations, initiating a large-scale vibrational motion.

Fig. 10(a) shows the vibrational-state population of the cationic $\tilde{A}$ state calculated for the Franck-Condon transition from the ground state of the neutral CH_3I. In the calculation, the wave functions for both initial and final states are obtained by solving the one-dimensional, time-independent Schrödinger equation for the PEC (along C-I bond) approximated as Morse potentials using spectroscopic data.[42,58-60] The Franck-Condon factors determining the population of the vibrational levels v are calculated as $fc_v = \ < \Psi_o^{neutral} | \Psi_v^A >$.[73] The resulting distribution is centered at v=15, whereas the peak in the measured vibrational frequency [Fig. 9(b)] corresponds to somewhat lower states (v=7-9). Besides the limitations of the simple model used to estimate the vibrational distribution, a likely reason for this deviation is the vibrational redistribution occurring during the pump pulse, including losses via dissociation. It should be noted that the vibrational states with v>10 lie above the lowest dissociation limit $CH_3{}^+ + I(^2P_{3/2})$.

Fig. 10(b) displays the simulated time-dependent probability density of the vibrational wave packet resulting from the vibrational state population shown in Fig. 10(a), which is obtained by the field-free propagation of this wave packet on the $\tilde{A}$-state potential. The wave packet manifests a characteristic temporal evolution observed in numerous earlier calculations (see e.g.[10, 74-76]). The originally rather well-localized wave packet dephases (i.e., spreads out) on the time scale of ~1ps because of the broad distribution of vibrational states and, thus, noticeably different vibrational frequencies. This dephasing explains the fading of the oscillatory structure observed in Figs. 4 and 5. Within the present simple model considering the propagation on a single one-dimensional potential curve, the wave packet would revive at ~ 6 ps. The experimental analysis of the revival structure (or lack thereof) requires further studies. However, in contrast to earlier observations for diatomics,[10, 76] the overall averaged signal also decreases, as can be clearly seen from Fig. 9(a). There are a several possible reasons for this behavior. First, the reduction of the signal can be a consequence of the dependence of the $\tilde{A}$-state ionization probability on the internuclear separation $R_{C\text{-}I}$, which increases at large $R_{C\text{-}I}$ because of the decreasing energy gap between the initial and the final state PEC. As can be seen from Fig. 10(b), the wave packet extends to large $R_{C\text{-}I}$ at small delays, which is reflected by the pronounced oscillation of the expectation value of $R_{C\text{-}I}$. Second, rotational dynamics induced by the pump pulse can influence the signal on a comparable time scale.[49, 77] Finally, the population losses due to dissociation can also be a contributing factor. Even though the major dissociation pathways discussed in the previous section unfold on a much faster

time scale (reflected by the descending bands in Fig. 4-6), the contribution from the slower dissociation mechanisms also plays a role. Further studies are needed in order to quantitatively determine how much each of the above factors contribute to the reduction of the $\tilde{A}$ state signal in our pump-probe experiment.

Interestingly, the oscillatory structure reflecting the nuclear wave packet motion in the cationic $\tilde{A}$ state is not present in the delay-dependent KER for the doubly-charged (1,1) channel obtained using higher intensities of the pump and probe pulses [see Fig. 8(a)]. Moreover, in the projections onto the KER axis shown in Fig. 8(b), a pronounced minimum can be observed at a KER of ~3.5 eV, i.e., corresponding to the center of the oscillatory feature in Fig. 4(a) and 5(a). We interpret this as a signature of efficient dissociation of the $\tilde{A}$ state within the pump pulse at higher intensity. The $\tilde{A}$ state dissociates efficiently with one NIR photon at large $R_{\text{C-I}}$. In a more intense pulse, the effective time window, where the laser intensity is high enough to dissociate the molecule, can significantly exceed the 25 fs (FWHM) duration of our laser pulses. In good agreement with this hypothesis, we observe a similar disappearance of the signatures of $\tilde{A}$ state vibrations in the dissociative ionization with increased pump-pulse intensity.[62]

The signatures of $\tilde{A}$-state vibrations observed in the (1,1) channel in Figs. 4, 5, and 9 indicate that at the intensity of 1.5×10^{14} W/cm^2, (i) the $\tilde{A}$-state population constitutes a non-negligible fraction of the bound cations (i.e., the ionization from the HOMO-1 orbital plays an important role), and (ii) that sequential double ionization proceeding via the cationic $\tilde{A}$ state can contribute significantly to the dissociative double ionization. The formation of the excited-state cations is important for the discussion of different KER values reported for this channel in earlier studies, which was briefly addressed at the end of section 3.2.1. For longer pulses used in[34, 41] (180 and 100 fs, respectively), the nuclear wave packet created in the $\tilde{A}$ state has enough time to propagate towards larger internuclear separations, resulting in KER values of 3.7 – 4 eV, which fall within the $\tilde{A}$-state band observed in the present work. In contrast, for shorter (50 fs) pulses as used, e.g., in[36, 38], the dynamics in the intermediate $\tilde{A}$ state do not play a role.

The KER value expected for a vertical (instantaneous) CE of the molecule at the equilibrium distance of the $\tilde{A}$ state is 5.9 eV. However, because of the population of higher vibrational states, the expectation value for $R_{C\text{-}I}$ of the vibrational wave packet for large delays settles at a larger $R_{C\text{-}I}$ value, which corresponds to a KER of 4.77 eV within the CE model. Nevertheless, even this KER value is significantly higher than the KER at which the oscillatory structure is observed. This can be readily explained by the deviation of the final-state PEC from Coulombic ones discussed in[36] and by the larger $\tilde{A}$-state ionization probability at large internuclear distances. The dominant contribution from the delay-independent bands above 4 eV, which is produced by either the pump or the probe pulse alone, prevents more detailed analysis of this issue (1,1) channel.

3.3. Pump-probe delay dependence of the $CH_3^+ + I^{++}$ channel

Although triple ionization is significantly weaker than double ionization at the laser intensities considered here, our data still contains a significant amount of triple ionization events that can be analyzed in order to verify our findings using a different final charge state reached in the probe step, namely the $CH_3^+ + I^{++}$ channel. Fig. 11(a) shows the delay dependence of the KER distribution for this channel obtained in the same measurement as the results shown in Fig. 4-7, i.e., for the pump and probe intensity of 1.5×10^{14} W/cm^2. A pronounced oscillatory structure appears in the KER range between 6 and 10 eV. Fig. 12 shows the projection of the coincident ion

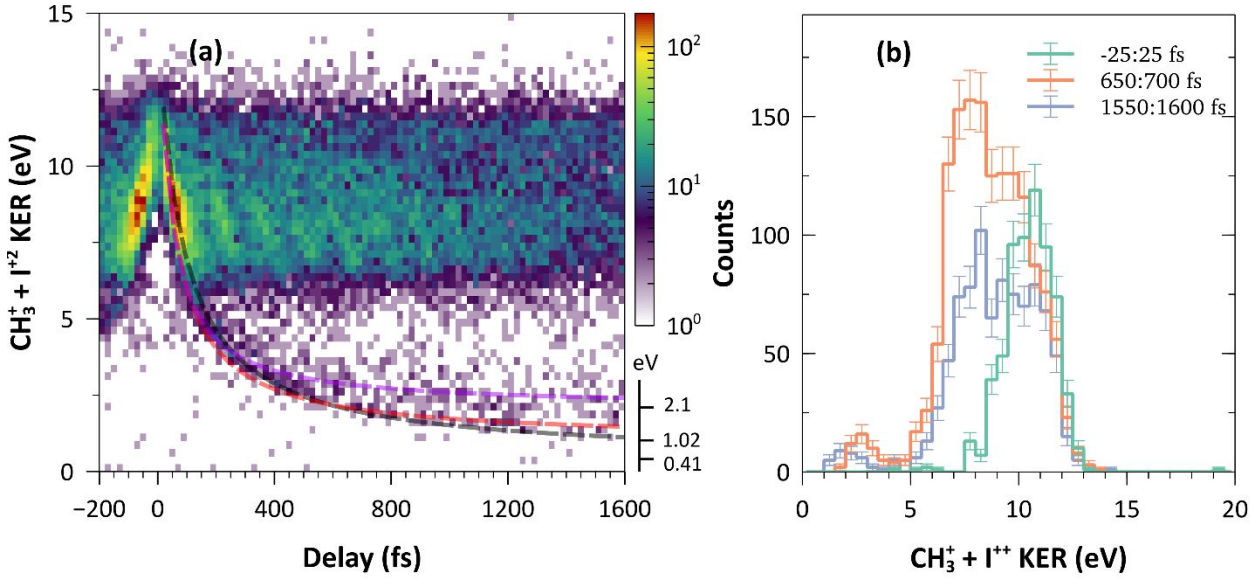

Fig. 11: Same as Fig. 4 but for the $CH_3^+ + I^{++}$ channel.

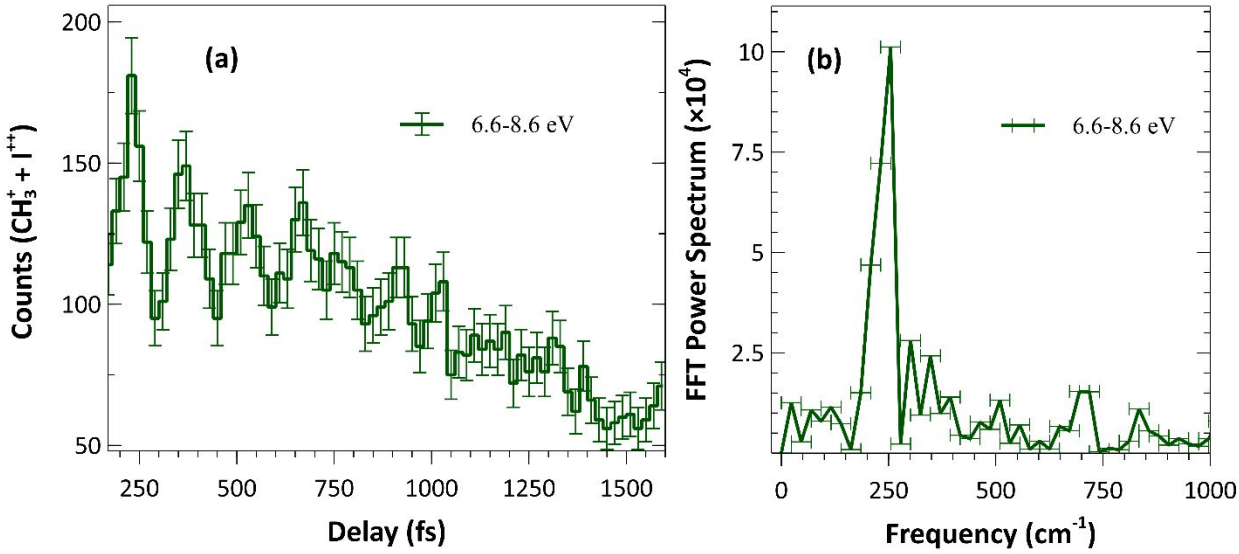

Fig. 12: Same as Fig. 8 but for the $CH_3^+ + I^{++}$ channel.

yield in that KER range on the delay axis and the corresponding FFT power spectrum, which has a pronounced peak slightly above 250 cm^{-1}. Similar to the frequency that has been discussed above for the $CH_3^+ + I^+$ channel, this also indicates that the pump pulse is preparing a wave packet on the $\tilde{A}$ state of CH_3I^+. However, in the probe step, the temporal evolution of this wave packet is mapped by a transition to the higher-lying $CH_3^+ + I^{++}$ PEC. The advantage of this probe scheme can be clearly seen in Fig. 11(a): since triple ionization by a single pulse is rather small at this intensity, the pump-probe signal reflecting the vibrational wave-packet motion in the cationic $\tilde{A}$ state yields the dominant contribution to the spectrum. Therefore, the dephasing of the wave packet becomes even more visible, and one can identify the upper limit for the KER stripes reflecting the vibrational motion, which is hidden by the delay-independent bands in Fig. 4-6. As can be seen in Fig. 12(a), besides dephasing, the overall signal resulting from the $\tilde{A}$ state wave packet decreases with increasing delays, similar to the $CH_3^+ + I^+$ (1,1) channel in Fig. 8(a). Since both channels reflect the motion of the same vibrational wave packet, the most likely reasons for this decrease are the same as those discussed in the previous section for the (1,1) channel.

The data presented in Fig. 11 along with the results of the simulation shown in Fig. 10(b) provide an intuitive, quantitative illustration how the CEI technique maps the structure of a particular nuclear wave packet into the delay-dependent KER. The wave packet in Fig. 10(b) is confined between 4 a.u. and ~9 a.u. Assuming that the ionization to the triply charged final state is instantaneous and that this state is purely Coulombic, we would expect the resulting KER to range from 13.6 eV to 6 eV. However, as it was shown in[36], CH_3I breakup upon triple ionization close to the equilibrium distance of the neutral molecule (which essentially coincides with the 4 a.u. innermost boundary of the cationic $\tilde{A}$ state wave packet) results in a KER peaking slightly above 10 eV because of the non-Coulombic nature of the tricationic PEC. This matches well with the KER measured in our experiment in the region where the pump and the probe pulses overlap [green curve in Fig. 11(b)] and where the dynamics in the intermediate state do not play an important role. The oscillatory structure reflecting vibrational motion in the cationic $\tilde{A}$ state extends from 10 eV down to ~6 eV. A good agreement between the latter value and the KER expected for the

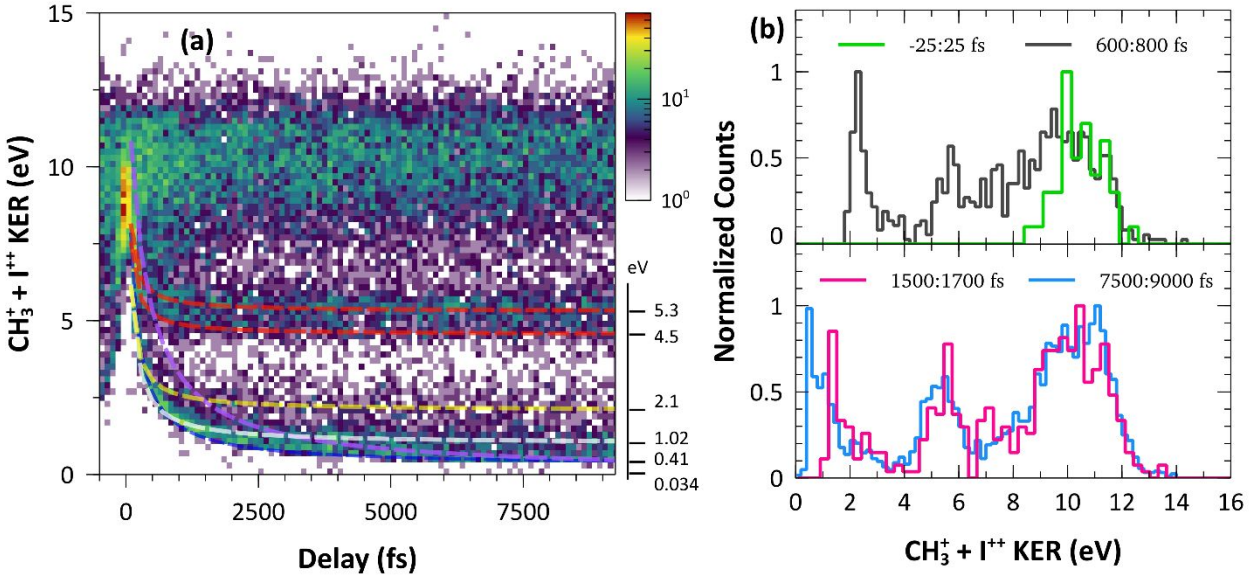

Fig. 13: Same as Fig. 8 but for the $CH_3^+ + I^{++}$ channel**.** For better visibility, the four KER distributions at different delays shown in (b) are split into two panels.

outermost region of the $\tilde{A}$ state wave packet within the simple CE model reflects the fact that at large C-I distances, the tricationic PEC becomes nearly Coulombic, as shown by the calculation presented in[36].

Here too, the oscillatory structure is not present in the results obtained using more intense pump and probe pulses [Fig. 13(a)], confirming that the cationic $\tilde{A}$ state is unlikely to survive during the pump pulse at 4×10^{14} W/cm^2 without undergoing dissociation. In comparison with the low-intensity data of Fig. 11(a), the spectrum in Fig. 13(a) shows a stronger delay-independent band centered around 10.8 eV, resembling the peak observed for zero-delay region in Fig. 11, and matching closely the KER value of 10.2 eV reported for the same channel by Corrales *et al*.[36] The higher-intensity data also shows a stronger contribution from dissociating wave packets in singly and doubly charged states produced by the pump pulse and promoted to the $CH_3^+ + I^{++}$ final state by the probe pulse. At long delays, the low-energy bands due to dissociation in the singly charged states approach the same asymptotic values as the descending bands in Fig. 4-6. The feature resulting from dissociative double ionization [simulated by the red lines in Fig. 13(a)] reaches much higher asymptotic values corresponding to the KER of the $CH_3^+ + I^+$ channel.

4. Conclusions

In this work, the ionization, dissociation and Coulomb explosion of CH_3I molecules induced by intense, 790-nm, 25-fs laser pulses is investigated by means of time-resolved coincident ion momentum imaging. By analyzing the kinetic energies and angular distributions of coincident ion pairs resulting from two-body breakup of doubly and triply charged CH_3I states as a function of pump-probe delay, we map the nuclear wave packet motion in several dissociation channels as well as in the bound cationic $\tilde{A}$ state. This state is identified as an important intermediate for dissociative ionization and sequential multiple ionization, which can, in sufficiently long laser pulses, result in Coulomb explosion at internuclear distances that are significantly larger than the equilibrium distance of the neutral molecule. Together with the non-Coulombic shape of the dicationic and trication potential energy curves near the equilibrium internuclear distance, our findings resolve the apparent contradiction between previous results for the strong-field induced Coulomb explosion of CH_3I that are reported in the literature. An oscillatory structure resulting from vibrational motion in the $\tilde{A}$ state, observed for pump and probe intensities of 1.5×10^{14} W/cm^2, dephases within ~1 ps, in qualitative agreement with the prediction of a simple wave packet propagation simulation. No signatures of such bound-state wave packet motion are observed at higher laser intensity of 4×10^{14} W/cm^2, indicating that under these conditions, the cations in the $\tilde{A}$ state are efficiently dissociated during the pump pulse.

The majority of the dissociative ionization channels studied in this work can be well understood in terms of initial ionization to the $\tilde{A}$ state and subsequent one- or two-photon transitions to one of the higher-lying repulsive curves. However, one observed channel with an asymptotic KER of ~2.1 eV and nearly isotropic angular distribution is not consistent with this scenario. While the

dominating mechanism populating this channel requires further investigation, it is evident from the results presented here that a combination of different, complementary experimental approaches significantly facilitates the reliable identification of different fragmentation pathways. The coincident ion imaging technique employed in this work yields asymptotic dissociation energies, reveals angular dependence of different channels, and, in a pump-probe scheme, provides information about the internuclear separation at a given time. However, this approach is not directly sensitive to the quantum state of a particular dissociation product, which can be determined, e.g., by transient absorption measurements.[29, 30, 42, 43] Therefore, one of the important remaining tasks for ultrafast photodissociation studies is to understand the relation between the asymptotic fragment kinetic energies, time-resolved CEI and photoelectron spectroscopy data, and characteristic time constants ("dissociation times") revealed by transient absorption measurements[43] or other state-sensitive probing techniques such as resonant multiphoton ionization.[78] Strong-field or single-photon-induced dissociation of CH_3I, which has been extensively studied with various experimental techniques, represents a promising test ground for establishing such a relation.

Acknowledgements

This work is supported by the Chemical Sciences, Geosciences, and Biosciences Division, Office of Basic Energy Sciences, Office of Science, US Department of Energy, Grant No. DE-FG02-86ER13491. We gratefully acknowledge Charles Fehrenbach for assistance with the laser operation; Kevin Carnes for help with the data acquisition; and the technical staff of JRML for support during the preparation of the experiment. We also acknowledge Max Sayler, Kevin Carnes, and other former and current members of Itzik Ben-Itzhak group for the development of the computer code to reconstruct lost delay-line signals, which was implemented in the data analysis for this paper. We also thank Wen Li for fruitful discussions.

Conflicts of interest

There are no conflicts of interest to declare.

Author contributions

Y.M., W.L.P., M.Z., B.K., K.R.P., and F.Z. carried out the pump-probe experiment, which was set up by Y.M., W.L.P. and M.Z. with guidance from I.B.I, D.R., and A.R. Y.M. wrote the data analysis code and analyzed and interpreted the data under the guidance of I.B.I., D.R., and A.R. and with input from all co-authors. S.X. performed the quantum chemistry and strong-field ionization calculations under the guidance of A.T.L. The manuscript was written by Y.M., D.R., and A.R. with input from all co-authors.

References

1. A. Zewail, *Angew. Chem. Int. Ed.*, 2000, **39**, 2586-2631.

2. J. H. Posthumus, *Rep. Prog. Phys.*, 2004, **67**, 623-665.

3. I.V. Hertel and W. Radloff, *Rep. Prog. Phys.*, 2006, **69**, 1897-2003.

4. A. Hishikawa, A. Iwamae, K. Hoshina, M. Kono and K. Yamanouchi, *Chem. Phys. Lett.*, 1998, **282**, 283–291.

5. J. H. Sanderson, A. El-Zein, W. A. Bryan, W. R. Newell, A. J. Langley and P. F. Taday, *Phys. Rev. A*, 1999, **59**, R2567-R2570.

6. F. Légaré, K. F. Lee, I. V. Litvinyuk, P. W. Dooley, S. S. Wesolowski, P. R. Bunker, P. Dombi, F. Krausz, A. D. Bandrauk, D. M. Villeneuve and P. B. Corkum, *Phys. Rev. A*, 2005, **71**, 013415.

7. J. Gagnon, K. F. Lee, D. M. Rayner, P. B. Corkum and V. R. Bhardwaj, *J. Phys. B*, 2008, **41**, 215104.

8. M. Pitzer, M. Kunitski, A. S. Johnson, T. Jahnke, H. Sann, F. Sturm, L. P. H. Schmidt, H. Schmidt-Böcking, R. Dörner, J. Stohner, J. Kiedrowski, M. Reggelin, S. Marquardt, A. Schießer, R. Berger and M. S. Schöffler, *Science*, 2013, **341**, 1096–1100.

9. Z. Vager, R. Naaman and E. P. Kanter, *Science*, 1989, **244**, 426-431.

10. T. Ergler, A. Rudenko, B. Feuerstein, K. Zrost, C. D. Schröter, R. Moshammer and J. Ullrich, *Phys. Rev. Lett.*, 2006, **97**, 193001.

11. A. Hishikawa, A. Matsuda, M. Fushitani and E. Takahashi, *Phys. Rev. Lett.*, 2007, **99**, 258302.

12. A. Matsuda, M. Fushitani, E. J. Takahashi and A. Hishikawa, *Phys. Chem. Chem. Phys.*, 2011, **13**, 8697-8704.

13. H. Ibrahim, B. Wales, S. Beaulieu, B. E. Schmidt, N. Thiré, E. P. Fowe, E. Bisson, C. T. Hebeisen, V. Wanie, M. Giguére, J.-C. Kieffer, M. Spanner, A. D. Bandrauk, J. Sanderson, M. S. Schuurman and F. Légaré, *Nat. Commun.*, 2014, **5**, 4422.

14. M. Burt, R. Boll, J.W.L. Lee, K. Amini, H. Köckert, C. Vallance, A. S. Gentleman, S. R. Mackenzie, S. Bari, C. Bomme, S. Düsterer, B. Erk, B. Manschwetus, E. Müller, D. Rompotis, E. Savelyev, N. Schirmel, S. Techert, R. Treusch, J. Küpper, S. Trippel, J. Wiese, H. Stapelfeldt, B. Cunha de Miranda, R. Guillemin, I. Ismail, L. Journel, T. Marchenko, J. Palaudroux, F. Penent, M. N. Piancastelli, M. Simon, O. Travnikova F. Brauβe, G. Goldsztejn, A. Rouzée, M. Geoleoc, R. Geneaux, T. Ruchon, J. Underwood, D. M. P. Holland, A. S. Mereshchenko, P. K. Olshin, P. Johnsson, S. Maclot, J. Lahl, A. Rudenko, F. Ziaee, M. Brouard and D. Rolles, *Phys. Rev. A*, 2017, **96**, 043415.

15. F. Allum, M. Burt, K. Amini, R. Boll, H. Köckert, P. K. Olshin, S. Bari, C. Bomme, F. Brauβe, B. Cunha de Miranda, S. Düsterer, B. Erk, M. Géléoc, R. Geneaux, A. S. Gentleman, G. Goldsztejn, R. Guillemin, D. M. P. Holland, I. Ismail, P. Johnsson, L. Journel, J. Küpper, J. Lahl,

J.W.L. Lee, S. Maclot, S. R. Mackenzie, B. Manschwetus, A. S. Mereshchenko, R. Mason, J. Palaudroux, F. Penent, M. N. Piancastelli, D. Rompotis, A. Rouzée, T. Ruchon, A. Rudenko, E. Savelyev, N. Schirmel, M. Simon, H. Stapelfeldt, S. Techert, O. Travnikova, S. Trippel, J. Underwood, C. Vallance, J. Wiese, F. Ziaee, M. Brouard, T. Marchenko and D. Rolles, *J. Chem. Phys.*, 2018, **149**, 204313.

16. S. J. Riley and K. R. Wilson, *Faraday Discuss. Chem. Soc.*, 1972, **53**, 132-146.

17. M. O. Hale, G. E. Galica, S. G. Glogover, and J. L. Kinsey, *J. Phys. Chem.*, 1986, **90**, 4997-5000.

18. Q. Zhu, J. R. Cao, Y. Wen, J. Zhang, X. Zhong, Y. Huang, W. Fang and X. Wu, *Chem. Phys. Lett.*, 1988, **144**, 486-492.

19. D. W. Chandler, J. W. Thoman Jr., M. H. M. Janssen and D. H. Parker, *Chem. Phys. Lett.*, 1989, **156**, 151-158.

20. Y. Amatatsu, K. Morokuma and S. Yabushita, *J. Chem. Phys.*, 1991, **94**, 4858-4876.

21. D. P. Zhong, P. Y. Cheng and A. H. Zewail, *J. Chem. Phys.*, 1996, **105**, 7864-7867.

22. A. T. J. B. Eppink and D. H. Parker, *J. Chem. Phys.*, 1998, **109**, 4758-4767.

23. D. P. Zhong and A. H. Zewail, *J. Phys. Chem. A*, 1998, **102**, 4031-4058.

24. A. T. J. B. Eppink and D. H. Parker, *J. Chem. Phys.*, 1999, **110**, 832-844.

25. R. de Nalda, J. Durá, A. García-Vela, J. G. Izquierdo, J. González-Vázquez and L. Bañares, *J. Chem. Phys.*, 2007, **126**, 021101.

26. J. Durá, R. de Nalda, J.Alvarez, J. G. Izquierdo, G. A. Amaral and L. Bañares, *Chem. Phys. Chem.*, 2008, **9**, 1245.

27. L. Rubio-Lago, A. Garcia-Vela, A. Arregui, G. A. Amaral and L. Banares, *J. Chem. Phys.*, 2009, **131**, 174309.

28. S. H. Gardiner, M. L. Lipciuc, T. N. V. Karsili, M. N. R. Ashfold, and C. Vallance, *Phys. Chem. Chem. Phys.*, 2015, **17**, 4096-4106.

29. A. R. Attar, A. Bhattacherjee, and S. R. Leone, *J. Phys. Chem. Lett.*, 2015, **6**, 5072-5077.

30. L. Drescher, M. C. E. Galbraith, G. Reitsma, J. Dura, N. Zhavoronkov, S. Patchkovskii, M. J. J. Vrakking, and J. Mikosch, *J. Chem. Phys.*, 2016, **145**, 011101.

31. M. Murillo-Sánchez, S. Marggi Poullain, J. González-Vázquez, G. Corrales, M. E. Balerdi, and L. Bañares, *Chem. Phys. Lett.*, 2017, **683**, 22-28.

32. F. Brauβe, G. Goldsztejn, K. Amini, R. Boll, S. Bari, C. Bomme, M. Brouard, M. Burt, B. Cunha de Miranda, S. Düsterer, B. Erk, M. Geoleoc, R. Geneaux, A. S. Gentleman, R. Guillemin, I. Ismail, P. Johnsson, L. Journel, T. Kierspel, H. Köckert, J. Küpper, P. Lablanquie, J. Lahl, J.W.L. Lee, S. R. Mackenzie, S. Maclot, B. Manschwetus, A. S. Mereshchenko, T. Mullins, P. K. Olshin,

J. Palaudroux, S. Pattchkovskii, F. Penent, M. N. Piancastelli, D. Rompotis, T. Ruchon, A. Rudenko, E. Savelyev, N. Schirmel, S. Techert, O. Travnikova S. Trippel, J. G. Underwood, C. Vallance, J. Wiese, M. Simon, D. M. P. Holland, T. Marchenko, A. Rouzée and D. Rolles, *Phys. Rev. A*, 2018, **97**, 043429.

33. P. Graham, K. W. D. Ledingham, R. P. Singhai, S. M. Hankin, T. Mc-Canny, X. Fang, C. Kosmidis, P. Tzallas, P. F. Taday and A. J. Langley, *J. Phys. B*, 2001, **34**, 4015.

34. H. Liu, Z. Yang, Z. Gao and Z. Tang, *J. Chem. Phys.*, 2007, **126**, 044316.

35. Y. Wang, S. Zhang, Z. Wei and B. Zhang, *J. Phys. Chem. A*, 2008, **112**, 3846-3851.

36. M. E. Corrales, G. Gitzinger, J. González-Vázquez, V. Loriot, R. de Nalda and L. Bañares, *J. Phys. Chem. A*, 2012, **116**, 2669-2677.

37. M. E. Corrales, J. González-Vázquez, G.Balerdi, I.R. Sola, R. de Nalda and L. Bañares, *Nat. Chem.*, 2014, **6**, 785-790.

38. S. K. Lee, F. Cudry, Y. F. Lin, S. Lingenfelter, A. H. Winney, L. Fan and W. Li, *Rev. Sci. Instr.*, 2014, **85**, 123303.

39. S. G. Walt, N. B. Ram, A. von Conta, O. I. Tolstikhin, L. Bojer Madsen, F. Jensen and H. J. Wörner, *J. Phys. Chem. A*, 2015, **119**, 11772–11782.

40. M. E. Corrales, R. de Nalda and L. Bañares, *Nat. Commun.*, 2017, **8**, 1345.

41. D. Zhang, S. Luo, H. Xu, M. Jin, F. Liu, B. Yan, Z. Wang, H. Liu, D. Jiang, A. Eppink, W. Roeterdink, S. Stolte and D. Ding, *Eur. Phys. J. D*, 2017, **71**, 148.

42. Z. Wei, J. Li, L. Wang, S. T. See, M. H. Jhon, Y, Zhang, F. Shi, M. Yuang and Z.-H. Loh, *Nat. Commun.*, 2017, **8**, 735.

43. Z. Wei, J. Li, S. T. See and Z.-H. Loh, *J. Phys. Chem. Lett.*, 2017, **8**, 6067-6072.

44. S. Luo, W. Hu, J. Yu, X. Li, L. He, C. Wang, F. Liu and D. Ding, *J. Phys. Chem. A*, 2017, **121,** 6547–6553.

45. S. Luo, S. Zhou, W. Hu, X. Li, P. Ma, J. Yu, R. Zhu, C. Wang, F. Liu, B. Yan, A. Liu, Y. Yang, F. Guo and D. Ding, *Phys. Rev. A*, 2017, **96**, 063415.

46. A.H. Winney, G. Basnayake , D. A. Debrah , Y. F. Lin, S. K. Lee, P. Hoerner, Q. Liao, H. B. Schlegel and W. Li, *J. Phys. Chem. Lett.*, 2018, **9**, 2539-2545.

47. K. Motomura, E. Kukk, H. Fukuzawa, S.-i. Wada, K. Nagaya, S. Ohmura, S. Mondal, T. Tachibana, Y. Ito, R. Koga, T. Sakai, K. Matsunami, A. Rudenko, C. Nicolas, X.-J. Liu, C. Miron, Y. Zhang, Y. Jiang, J. Chen, M. Anand, D. Eon Kim, K. Tono, M. Yabashi, M. Yao and K. Ueda, *J. Phys. Chem. Lett.*, 2015, **6**, 2944-2949.

48. A. Rudenko, L. Inhester, K. Hanasaki, X. Li, S.J. Robatjazi, B. Erk, R. Boll, K. Toyota, Y. Hao, O. Vendrell, C. Bomme, E. Savelyev, B. Rudek, L. Foucar, S.H. Southworth, C.S. Lehmann,

B. Kraessig, T. Marchenko, M. Simon, K. Ueda, K.R. Ferguson, M. Bucher, T. Gorkhover, S. Carron, R. Alonso-Mori, J.E. Koglin, J. Correa, G.J. Williams, S. Boutet, L. Young, C. Bostedt, S.-K. Son, R. Santra and D. Rolles, *Nature*, 2017, **546**, 129-132.

49. B. Erk, R. Boll, S. Trippel, D. Anielski, L. Foucar, B. Rudek, S.W. Epp, R. Coffee, S. Carron, S. Schorb, K.R. Ferguson, M. Swiggers, J.D. Bozek, M. Simon, T. Marchenko, J. Küpper, I. Schlichting, J. Ullrich, C. Bostedt, D. Rolles and A. Rudenko, *Science*, 2014, **345**, 288-291.

50. R. Boll, B. Erk, R. Coffee, S. Trippel, T. Kierspel, C. Bomme, J.D. Bozek, M. Burkett, S. Carron, K. R. Ferguson, L. Foucar, J. Küpper, T. Marchenko, C. Miron, M. Patanen, T. Osipov, S. Schorb, M. Simon, M. Swiggers, S.Techert, K. Ueda, C. Bostedt, D. Rolles and A. Rudenko, *Struct. Dyn.*, 2016, **3**, 043207.

51. K. Amini, E. Savelyev, F. Brauβe, N. Berrah, C. Bomme, M. Brouard, M. Burt, L. Christensen, S. Düsterer, B. Erk, H. Höppner, T. Kierspel, F. Krecinic, A. Lauer, J.W.L. Lee, M. Müller, E. Müller, T. Mullins, H. Redlin, N. Schirmel, S. Techert, J. Thørgersen, S. Toleikis, R. Treusch, S. Trippel, A. Ulmer, C. Vallance, J. Wiese, P. Johnsson, J. Küpper, A. Rudenko, A. Rouzée, H. Stapelfeldt, D. Rolles and R. Boll, *Struct. Dyn.*, 2018, **5**, 014301.

52. R. de Nalda, J. Durá, A. García-Vela, J. G. Izquierdo, J. González-Vázquez and L. Bañares, *J. Chem. Phys.*, 2008, **128**, 244309.

53. J. Durá, R. de Nalda, G. A. Amaral and L. Bañares, *J. Chem. Phys.*, 2009, **131**, 134311.

54. A. García-Vela, R. de Nalda, J. Durá, J. González-Vázquez and L. Bañares, *J. Chem. Phys.*, 2011, **135**, 154306.

55. J. Ullrich, R. Moshammer, R. Dörner, O. Jagutzki, V. Mergel, H. Schmidt-Böcking and L. Spielberger, *J. Phys. B: At. Mol. Opt. Phys.*, 1997, **30,** 2917-2974.

56. R. Dörner, V. Mergel, O. Jagutzki, L. Spielberger, J. Ullrich, R. Moshammer and H. Schmidt-Böcking, *Phys. Rep.*, 2000, **330**, 95–192.

57. J. Ullrich, R. Moshammer, A. Dorn, R. Dörner, L. P. H. Schmidt and H. Schmidt-Böcking, *Rep. Prog. Phys.*, 2003, **66**, 1463-1545.

58. K. Walter, R. Weinkauf, U. Boesl and E.W. Schlag, *J. Chem. Phys.*, 1988, **89**, 1914-1922.

59. *NIST Chemistry WebBook, Standard Reference Database Number 69*; DOI: https://doi.org/10.18434/T4D303 .

60. Y. J. Bae and M. S. Kim, Chem. *Chem. Phys. Chem.*, 2008, **9**, 1709-1714.

61. F. Aquilante *et al*., *J. Comput. Chem.*, 2015, **37**, 506.

62. Y. Malakar, S. Xue, B. Kaderiya, W.L. Pearson, M. Zohrabi, Kanaka Raju P., F. Ziaee, I. Ben-Itzhak, A.T. Le, D. Rolles and A. Rudenko, *in preparation*, 2018.

63. X. Ren, A M Summers, Kanaka Raju, A. Vajdi, V. Makhija, C W Fehrenbach, N. G Kling, K J Betsch, Z Wang, M F Kling, K D Carnes, I Ben-Itzhak, C. Trallero-Herrero and V. Kumarappan, *J. Optics*, 2017, **19**, 124017.

64. C. M. Maharjan, *Momentum Imaging Studies of Electron and Ion dynamics in a Strong Laser Field.* PhD thesis, Kansas State University, 2007.

65. A. Rudenko, K. Zrost, C. D. Schröter, V.L.B. de Jesus, B. Feuerstein, R. Moshammer and J. Ullrich, *J. Phys. B: At. Mol. Opt. Phys.*, 2004, **37**, L407-L413.

66. B. Jochim, R. Erdwien, Y. Malakar, T. Severt, B. Berry, P. Feizollah, J. Rajput, B. Kaderiya, W.L. Pearson, K.D. Carnes, A. Rudenko and I. Ben-Itzhak, *New J. Phys.*, 2017, **19**, 103006.

67. Th. Ergler, A. Rudenko, B. Feuerstein, K. Zrost, C. D. Schröter, R. Moshammer and J. Ullrich, *Phys. Rev. Lett.*, 2005, **95**, 093001.

68. C.R. Calvert, W.A. Bryan, W.R. Newell and I.D. Williams, *Physics Reports*, 2010, **491**, 1-28.

69. S. De, M. Magrakvelidze, I. A. Bocharova, D. Ray, W. Cao, I. Znakovskaya, H. Li, Z. Wang, G. Laurent, U. Thumm, M. F. Kling, I. V. Litvinyuk, I. Ben-Itzhak and C. L. Cocke, *Phys. Rev. A*, 2011, **84**, 043410.

70. P. Hoerner and H. B. Schlegel, *J. Phys. Chem. A*, 2017, **121**, 5940-5946.

71. R. N. Zare, *J. Chem. Phys.*, 1967, **47**, 204-215.

72. M. Tadjeddine, G. Bouchoux, L. Malegat, J. Durup, C. Pernot and J. Weiner, *Chem. Phys.*, 1982, **69**, 229-246.

73. B. H. Bransden and C. J. Joachain, *Physics of Atoms and Molecules*, 2nd ed., New York: Prentice-Hall, 2003.

74. B. Feuerstein and U. Thumm, *Phys. Rev. A*, 2003, **67**, 063408.

75. A. Alnaser, B. Ulrich, X. M. Tong, I. V. Litvinyuk, C. M. Maharjan, P. Ranitovic, T. Osipov, R. Ali, S. Ghimire, Z. Chang, C. D. Lin and C. L. Cocke, *Phys. Rev. A*, 2005, **72**, 030702(R).

76. L. Fang and G.N. Gibson, *Phys. Rev. A*, 2007, **75**, 063410.

77. E. Hamilton, T. Seideman, T. Ejdrup, M.D. Poulsen, C.Z. Bisgaard, S.S. Viftrup and H. Stapelfeldt, *Phys. Rev. A*, 2005, **72**, 043402.

78. M.E. Corrales, V. Loriot, G. Balerdi, J. Gonzalez-Vazquez, R. de Nalda, L. Banares and A.H. Zewail, *Phys. Chem. Chem. Phys.*, 2014, **16**, 8812-8818.

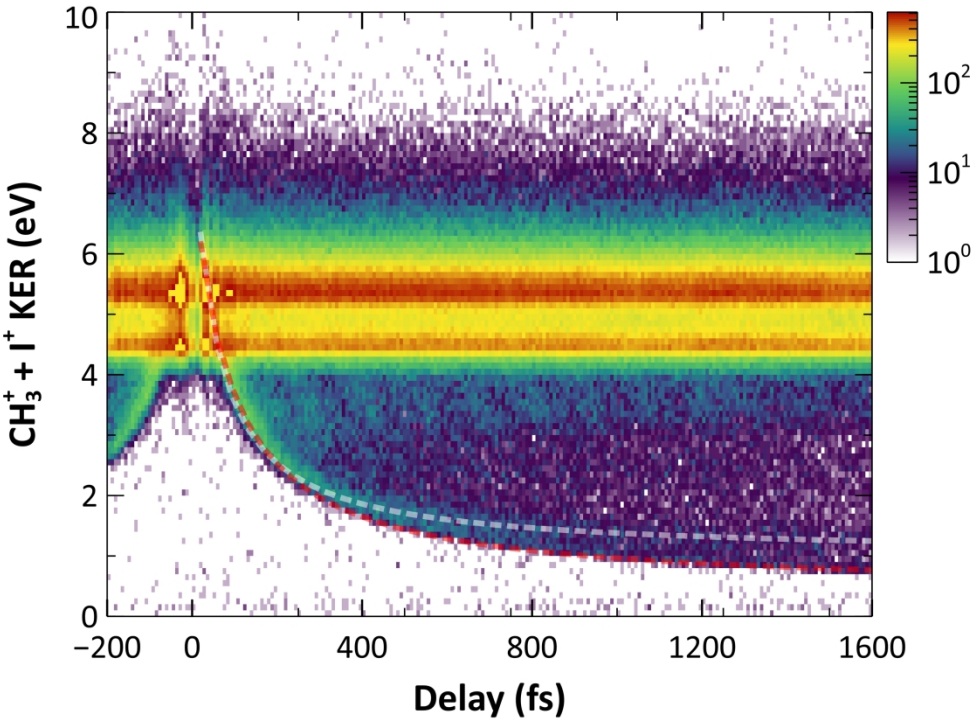

124x90mm (600 x 600 DPI)